Hindawi
International Journal of Energy Research
Volume 2024, Article ID 9953038, 12 pages
https://doi.org/10.1155/2024/9953038

Research Article

Substantial Electrocatalytic Oxygen Evolution Performances of Activated Carbon-Decorated Vanadium Pentoxide Nanocomposites

Sankar Sekar,[1,2] Pugazhendi Ilanchezhiyan,[2] Abu Talha Aqueel Ahmed,[1] Youngmin Lee,[1,2] and Sejoon Lee[1,2]

[1]*Division of System Semiconductor, Dongguk University-Seoul, Seoul 04620, Republic of Korea*
[2]*Quantum-Functional Semiconductor Research Center, Dongguk University-Seoul, Seoul 04620, Republic of Korea*

Correspondence should be addressed to Sejoon Lee; sejoon@dongguk.edu

Received 13 March 2024; Revised 9 April 2024; Accepted 20 April 2024; Published 8 May 2024

Academic Editor: Suresh Kannan Balasingam

Developing the ecofriendly and high-fidelity electrocatalysts for the oxygen evolution reaction (OER) is essential to foster effective production of environmentally friendly hydrogen. Herein, we fabricated the highly efficient OER electrocatalysts of the activated carbon-decorated vanadium pentoxide (AC-V_2O_5) nanocomposites using a facile hydrothermal technique. The AC-V_2O_5 nanocomposites displayed an aggregated structure of the AC nano-sheet-anchored orthorhombic V_2O_5 nanorods. When performing the OER process in an alkaline electrolyte at 10 mA/cm^2, AC-V_2O_5 exhibited the low overpotential (~230 mV), small Tafel slope (~54 mV/dec), and excellent stability. These substantial OER performances of AC-V_2O_5 could be ascribed to the synergistic effects from both the electrochemically active V_2O_5 nanorods and the highly conductive AC nanosheets. The results infer that the AC-V_2O_5 nanocomposites possess a substantial aptitude as a high-performance OER electrocatalyst for production of the future green energy source—hydrogen.

1. Introduction

Recently, continuously escalating demands and concerns about the energy, environment, and exhaustion of fossil fuels have spurred the energy science and technology communities to explore the ecofriendly renewable energy sources [1–3]. Among various energy sources, due to its natural abundance, high energy density, and zero carbon radiation, hydrogen (H_2) has emerged as a prominent resource for future green energy technology [4, 5]. For effective H_2 production, the electrocatalytic water-splitting technique is promising because of its excellent recyclability, extraordinary sustainability, and absence of pollution [6, 7]. In the overall water-splitting process, the oxygen evolution reaction (OER) activity is of great importance because of its sluggish reaction kinetics, attributed to the four-electron oxidative half-reaction [8, 9]. Currently, IrO_2- and RuO_2-based nanocomposites have been secured as an excellent OER electrocatalyst because of their supreme active sites and high H_2 production rates. However, the high cost, rareness, and fast deactivation of those rare earth metal oxides forcefully impede their wide applications [10, 11]. Therefore, developing the cost-effective, earth-abundant, and nonnoble OER electrocatalysts with a high water-to-hydrogen conversion efficiency is crucial.

As an alternative to the rare earth metal oxides, the semiconductive transition metal oxides are promising because of their high specific surface areas, modified electronic structures, enhanced interface tunability, and high electrochemical activity [12, 13]. Among them, vanadium pentoxide (V_2O_5) is favorable for demonstrating high OER performances because of its cost-effectiveness, simple synthesis process, layered structure, high redox-active sites, and intrinsically nonexplosive safe characteristics [14–17]. To obtain the high-quality V_2O_5 nanostructures, there are several synthesis methods such as sonochemical [18, 19], sol-gel [20], acid leaching [21], electrospinning [22, 23], laser irradiation [24], spray pyrolysis [25], hydrothermal [26–28], and chemical vapor deposition [29, 30]. When using bare V_2O_5 alone as an OER electrocatalyst, however, OER activity is rather meager because of its fast electron transmission, low electrical conductivity, scarce electrochemically active sites, and sluggish kinetics [10, 11, 17]. To improve the electrocatalytic OER performance of V_2O_5, therefore, decorating the V_2O_5 nanostructures with different transition metal oxides/chalcogenides [31–33] or various carbonaceous materials (e.g., graphene [34], reduced graphene oxide [15, 35], carbon nanotubes [36], graphitic carbon [18], and activated carbon (AC) [37]) was employed. Among them, AC possesses several advantages such as a variety of morphological architectures, facile synthesis methods, large specific surface areas, and superior electrical conductivity. Furthermore, the high-quality AC nanostructures could be derived from various biomass waste resources [38–40]; hence, biomass AC provides more advantages such as mass production, low cost, fast supply, and ecofriendliness [41–43]. Moreover, the morphological characteristics of AC could be modified when obtaining it through carbonization and activation of the biomass materials [44, 45]. Despite the above benefits, biomass AC-incorporated V_2O_5 has not been used as an OER electrocatalyst.

All those backgrounds prompt us to investigate the electrocatalytic characteristics of the biomass AC-encapsulated V_2O_5 (AC-V_2O_5) nanocomposites. Herein, we fabricated the high-performance electrocatalytic OER catalyst of AC-V_2O_5 by the facile hydrothermal aggregation process using the hydrothermally disassembled V_2O_5 and the biomass rice husk-derived AC nanosheets. The prepared AC-V_2O_5 catalyst exhibited the excellent OER activities with a low overpotential (~230 mV) and a small Tafel slope (~54 mV/dec). In this article, the material characteristic-to-electrocatalytic performances are meticulously analyzed and discussed.

2. Experimental Section

2.1. Materials. For the hydrothermal synthesis of the V_2O_5 nanorods, the commercial bulk V_2O_5 powder, ethanol (C_2H_6O), and potassium hydroxide (KOH) were purchased from Sigma-Aldrich (St. Louis, MO, USA); and those were used with no additional purification. In the case of biomass AC, brown rice husks, which had been collected from Tamil Nadu (India), were used as a source material. In all the experiments, deionized (DI) water was employed to avoid chemical contamination.

2.2. Preparation of V_2O_5 Nanorods. Figure 1 represents the experimental steps for fabricating the AC-V_2O_5 nanocomposites. As a primary step, the V_2O_5 nanorods were prepared by the hydrothermal disassembly process using the bulk V_2O_5 power. Initially, 0.5 g of V_2O_5 was mixed in 70 ml of DI water by stirring for 20 min at room temperature (25°C). Next, the above aqueous solution was transferred to the Teflon autoclave (100 ml), and then, the hydrothermal disassembly was performed in an electric oven at 150°C for 6 h. Thereafter, the autoclave chamber was cooled to 25°C, and then, the hydrothermally disassembled V_2O_5 nanorods were gathered and rinsed with DI water and C_2H_6O to remove other contaminants that might be introduced during the sample manipulation. Finally, the V_2O_5 nanorods were obtained in nanopowder form by drying the above colloidal suspension at 120°C for 8 h.

2.3. Derivation of Biomass AC Nanosheets. The biomass AC nanosheets were derived from the brown rice husks through the following process. Firstly, the raw rice husks were cleaned with DI water and dehydrated for 100 h in an air atmosphere. Then, the dried rice husks were carbonized in a muffle furnace at 400°C for 1 h. After collecting 3 g of carbonized rice husk ashes in a mortar, 12 g of KOH was mixed to carry out the KOH activation process. The mixture was then put into the alumina crucible and annealed at 600°C for 2 h. Next, the KOH-activated rice husk ashes were stirred in 100 ml of DI water to get rid of other traces of potassium-related residues. Finally, the cleaned suspension was filtrated and dried at 100°C for 12 h to collect the AC nanosheets in powder form.

2.4. Fabrication of AC-V_2O_5 Nanocomposites. The AC-V_2O_5 composites were prepared by the hydrothermal reassembly process using the above V_2O_5 nanorods and AC nanosheets. Initially, 0.5 g of V_2O_5 nanorods was dissolved in 70 ml of DI water and stirred for 20 min at room temperature (25°C). Then, 0.25 g of biomass AC nanosheets was added into the V_2O_5-mixed aqueous solution. After stirring it for 20 min, the AC-V_2O_5 mixture solution was transferred to the Teflon autoclave (100 ml) to conduct the hydrothermal reassembly process. Soon after the hydrothermal treatment at 150°C for 6 h, the autoclave chamber was cooled to 25°C to collect the aggregated composites of AC-V_2O_5. The collected AC-V_2O_5 wet powder was filtered and cleaned three times by C_2H_6O and DI water to remove the unreacted traces. After drying the cleaned AC-V_2O_5 wet powder at 120°C for 8 h, finally, the nanopowder type of AC-V_2O_5 was obtained.

2.5. Material Characterization. The morphological and the compositional properties of V_2O_5 and AC-V_2O_5 were studied by means of field emission scanning electron microscopy (FE-SEM, Inspect-F50, FEI, Mahwah, NJ, USA) and in situ energy-dispersive X-ray (EDX) spectroscopy, respectively. The vibrational and the crystallographic characteristics were analyzed by Raman scattering spectroscopy (LabRAM HR-800, Jobin Yvon, Longjumeau, France) and X-ray diffractometry (XRD, D8-Advance, Bruker, USA), respectively. Furthermore, the chemical bonding states of AC-V_2O_5 were further investigated by X-ray photoelectron spectroscopy (XPS) using a ESCALab250Xi system (Thermo Fisher Scientific, USA).

2.6. Measurements of Electrocatalytic OER Characteristics. The electrocatalytic OER performances of V_2O_5 and AC-V_2O_5 were investigated through the electrochemical characterization using the three-electrode measurement setup with a VersaSTAT-3 workstation (Ametek Scientific Instruments, Berwyn, PA, USA). Initially, we fabricated two different working electrodes using V_2O_5 and AC-V_2O_5. For this, the prepared catalyst (i.e., either V_2O_5 or AC-V_2O_5) was blended with the N-methyl-2-pyrrolidinone solution and

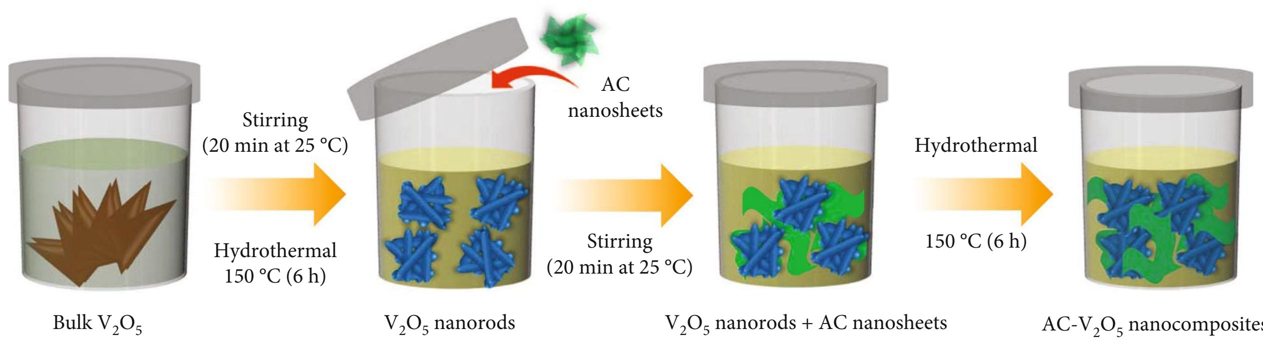

Figure 1: Experimental procedures for the fabrication of the V_2O_5 nanorods and the AC-V_2O_5 nanocomposites.

coated onto the nickel foam substrate (1 cm^2). Then, each catalyst-coated nickel foam substrate was dried individually at 180°C for 6 h. The alkaline KOH (1 M) solution was used as an electrolyte source for the OER measurements. Additionally, the Pt mesh electrode and the saturated calomel electrode (SCE) were also used as a counter electrode and a reference electrode, respectively. After preparing all the required electrodes, the cyclic voltammetry (CV) characteristics were assessed at different scan rates of 10–100 mV/s within a potential range from 0 to 0.5 V. In addition, the linear sweep voltammetry (LSV) measurements were conducted in −0.1–1.0 V potential ranges at a constant scan rate of 1.0 mV/s. To investigate the electrical characteristics of V_2O_5 and AC-V_2O_5, the electrochemical impedance spectroscopy (EIS) responses were measured at 1 Hz–10 kHz with the 10 mV amplitude of the applied AC signal. Furthermore, the chronopotentiometric (CP) characteristics of the samples were examined by applying stepwise current (i.e., $10 \longrightarrow 20 \longrightarrow 30 \longrightarrow 40 \longrightarrow 50 \longrightarrow 100\ mA/cm^2$ (for 10 min at each step)).

3. Results and Discussion

Figure 2 displays the morphological features of V_2O_5 and AC-V_2O_5. The bare V_2O_5 nanorods exhibited the aggregated morphology with plenty of nanorods (Figures 2(a) and 2(b)). The formation of V_2O_5 nanorods can be explained by hydrothermal cleaving and dispersing the layer-structured V_2O_5 stacks [46–51]. Since bulk V_2O_5 is composed of bunch of stacked layers (Figure S1), they can be effectively broken into the smaller species. Namely, during the hydrothermal process in a closed autoclave medium, the hydroxyl (OH^*) and hydrogen (H^*) radicals will supply the boundaries of the layered V_2O_5 stacks with a sufficient energy to cleave themselves. Different from the bare V_2O_5 nanorods, the AC-V_2O_5 nanocomposites revealed the AC nanosheet-decorated V_2O_5 nanorods (Figures 2(c) and 2(d); see also Figure S2 for the morphological shape of the AC nanosheets). Namely, after hydrothermal hybridization of V_2O_5 and AC, most of the V_2O_5 nanorods were aggregated and encapsulated by the AC nanosheets. Next, the compositional properties of V_2O_5 and AC-V_2O_5 were confirmed by in situ EDX measurements. As shown in Figures 2(e) and 2(f), both samples displayed their own intrinsic species such as C, V, and O, indicating the high purity of the present materials. One additional peak from Au was arisen from the ultrathin coating layer utilized to minimize the electron charging behavior during the FE-SEM measurement of the oxide material.

The structural characteristics of V_2O_5 and AC-V_2O_5 were investigated by XRD measurements. As depicted in Figure 3(a), the V_2O_5 nanorods exhibited the diffraction patterns at 15.3, 20.2, 21.7, 26.2, 31.0, 32.3, 33.3, 34.2, 37.3, 41.1, 42.0, 45.4, 47.1, 48.9, 49.9, 51.9, 55.5, 58.4, 60.1, 62.1, 66.1, 68.8, 71.1, 72.4, and 76.1°, corresponding to the (200), (001), (110), (101), (400), (011), (111), (301), (211), (020), (120), (411), (600), (021), (002), (610), (012), (421), (312), (701), (230), (330), (621), (322), and (331) crystal planes of orthorhombic V_2O_5 (JCPDS card no: 86-2248), respectively [52, 53]. For the AC nanosheets (see Figure S3), the two typical patterns of (002) and (100) were found at 21.8° and 43.1°, respectively. In the case of AC-V_2O_5, the (001) peak was red-shifted by 6.2° because of the aggregation of amorphous AC and crystalline V_2O_5 during the hydrothermal reassembly process [54, 55]. However, no AC-related patterns were detected from AC-V_2O_5 because of the relatively lower diffraction intensity of AC than that of V_2O_5 [56, 57].

The molecular interactions of V_2O_5 and AC-V_2O_5 were further examined by Raman scattering spectroscopy. As can be seen from Figure 3(b), the V_2O_5 nanorods showed the ten structural vibrational bands at 102, 143, 197, 282, 300, 403, 482, 524, 700, and 995 cm^{-1}, associated with the orthorhombic structure of V_2O_5. The Raman modes at 102 and 143 cm^{-1} might be ascribed to the stretching vibrations of the V–O bond and the layered V_2O_5 structure [58], respectively. The Raman modes at 197 and 282 cm^{-1} could be accredited to the twisting vibrations of O–V–O with the chain translation in V_2O_5 [52]. The bands at 300 and 403 cm^{-1} are known to originate from the twisting vibrations of the V=O bonds [59]. The Raman mode at 482 cm^{-1} could be described as resulting from the elongating vibrations of the triply-coordinated V_3–O bonds, which are located on the oxygen atom edges shared by three pyramids. The Raman scattering modes at 524 and 700 cm^{-1} could be correlated with the twisting and stretching modes of the doubly synchronized V–O–V bonds, comprising the corner-shared oxygen atoms [60, 61]. The vibrational band at 995 cm^{-1} was sprouted from the elongating vibrations of the twofold V=O bonds, verifying the layered structure of V_2O_5 [62].

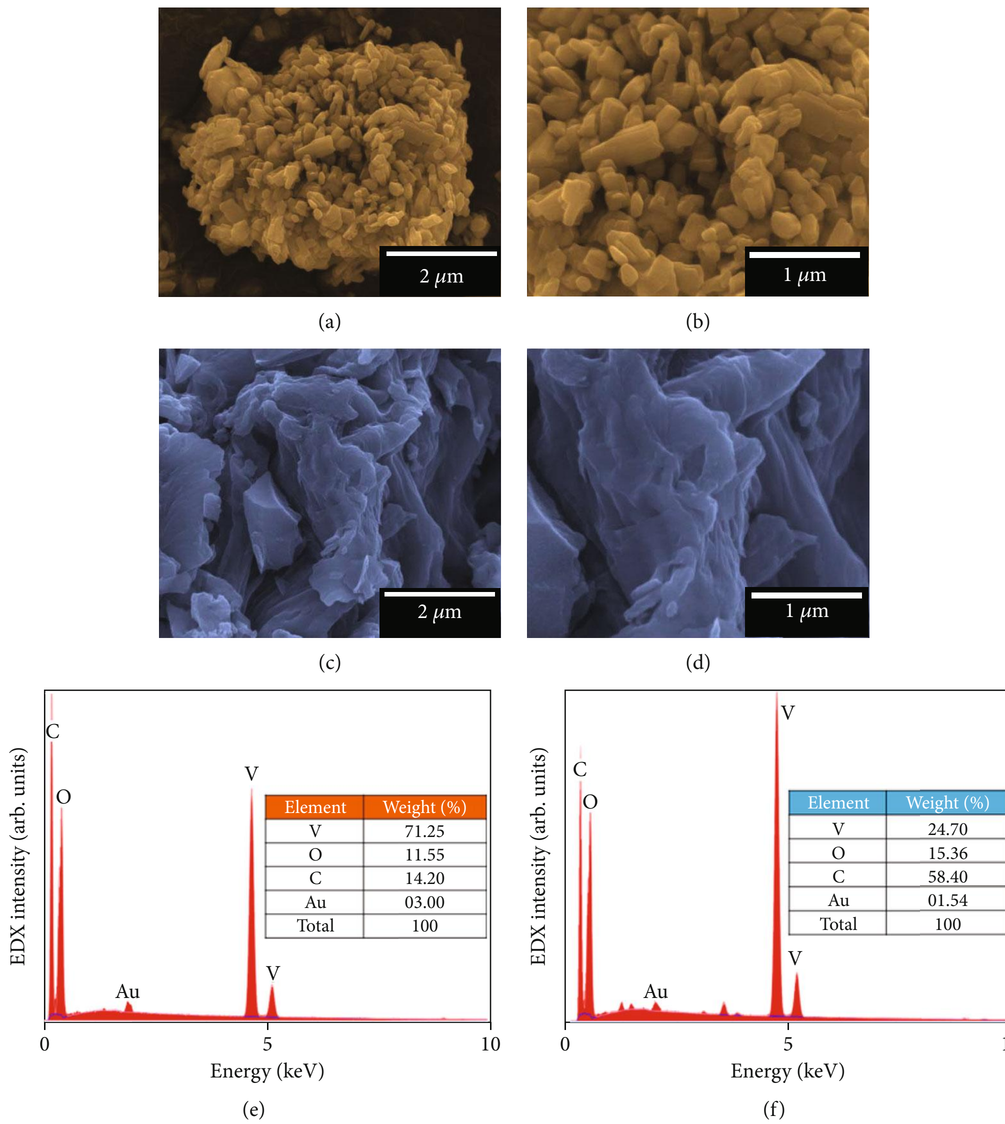

Figure 2: Microstructural and compositional characteristics of the V_2O_5 nanorods and the AC-V_2O_5 nanocomposites. (a) Low- and (b) high-magnification FE-SEM images of the V_2O_5 nanorods and (c) low- and (d) high-magnification FE-SEM images of the AC-V_2O_5 nanocomposites. EDX spectra of the (e) V_2O_5 nanorods and the (f) AC-V_2O_5 nanocomposites.

In the case of the AC nanosheets, we here note that two distinct Raman scattering modes were observed at 1354 and 1601 cm^{-1}, originating from the D and G bands of the layered AC nanosheets (see Figure S4) [40, 42, 57]. Consequently, the AC-V_2O_5 nanocomposites clearly revealed the relevant Raman features from both V_2O_5 and AC. Furthermore, the Raman bands of the AC-V_2O_5 nanocomposites were shifted to the lower wavenumber region than those of bare V_2O_5 because the incorporated amorphous AC led to the increase in the interlayer distance [10]. This specifies that V_2O_5 and AC were effectively hybridized in the AC-V_2O_5 nanocomposites system.

The hybridization of AC and V_2O_5 was further elucidated by the XPS measurements. As can be seen from the full-survey XPS spectra (Figure 4(a)), both catalysts revealed their own elements such as V, O, and C, whereas no other impurities were observed. In the case of bare V_2O_5, the core-level spectrum of V 2p exhibited the two peaks at 524.51 and 517.06 eV, corresponding to the V $2p_{1/2}$ and V $2p_{3/2}$ states, respectively (see Figure 4(b)) [36, 63]. Through deconvoluting these peaks, it was confirmed that V^{5+} and V^{4+} valence states coexisted in V_2O_5. Namely, the peaks at 515.28 and 522.64 eV could be attributed to the V^{4+} valence states, and the peaks at 516.99 and 524.47 eV could be ascribed to the V^{5+} valence state [36]. As can be confirmed from Figure 4(b), the portion of the pentaionized V^{5+} valence was dominant in V_2O_5, compared to V^{4+}. This specifies that the bonding states of V_2O_5 are chemically stable. For the O 1s case in bare V_2O_5 (Figure 4(c)), there are three O-related bonding states of O_I (530.04 eV), O_{II} (531.32 eV), and O_{III} (533.03 eV), which are well-known to correspond to the oxygen atoms bonded with the vanadium metal ions in the host V_2O_5 lattice, oxygen vacancies, and chemically adsorbed oxygen atoms at the surface, respectively [64, 65].

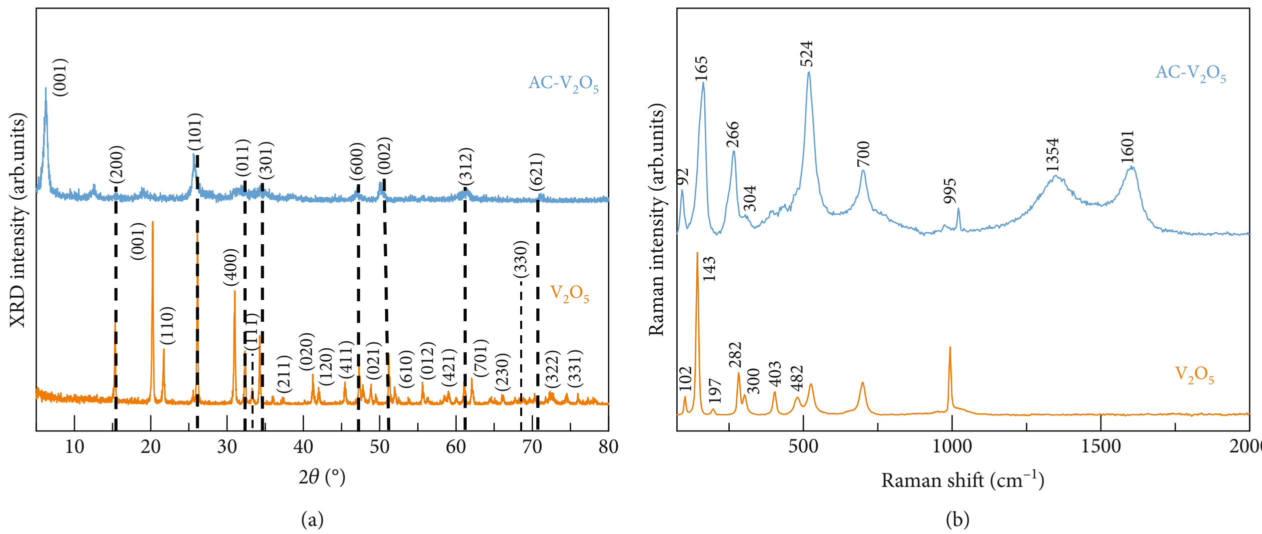

Figure 3: (a) XRD patterns of the V_2O_5 nanorods and the AC-V_2O_5 nanocomposites. (b) Raman spectra of the V_2O_5 nanorods and the AC-V_2O_5 nanocomposites.

Similar to those above in V_2O_5, the AC-V_2O_5 nanocomposites exhibited almost identical valence states in the V 2p core level (see Figure 4(d)). Compared to bare V_2O_5, however, there are two different features; i.e., one is the appearance of C-related bonds, and the other is the change in O-related bonds. As shown in Figure 4(e), AC-V_2O_5 clearly exhibited the existence of C-related bonds inside the composite material system. As deconvoluted, the C 1s involves the three bonding states centered at 288.93, 286.27, and 284.88 eV, attributing to the C=O, C–O, and C–C (sp^2 hybridized carbon) bonds, respectively [10, 57]. Furthermore, from the O 1s spectrum of AC-V_2O_5 (Figure 4(f)), one can clearly observe that the O-C bonds (i.e., O_{IV} at 532.17 eV [66]) were additionally included in the composite material system. Such an appearance of carbon-oxygen bonds (i.e., C=O and C–O in C 1s and O-C in O 1s) substantiates the effective hybridization of AC and V_2O_5 in the present composite system.

After confirming the effective hybridization of AC-V_2O_5, we examined the effects of the AC incorporation on the OER performances of AC-V_2O_5 because the synergistic effects from AC (i.e., high electrical conductivity) and V_2O_5 (i.e., high ion diffusivity) could be beneficial for enhancing the electrocatalytic OER performance. Figures 5(a) and 5(b) display the CV curves for V_2O_5 and AC-V_2O_5, respectively, measured under various scan rates ranging from 10 to 100 mV/s. Both samples exhibited the distinctive oxidation and reduction peaks, representing the Faradic redox-based pseudocapacitive activities of the prepared catalysts. When increasing the scan rate, the current density increased because of the low diffusion resistance. Compared to bare V_2O_5, AC-V_2O_5 exhibited the larger integrated CV windows. Furthermore, the AC-V_2O_5 catalyst exhibited the increased redox peak intensities, indicative of the restricted redox reaction in AC-V_2O_5. Namely, when incorporating AC into V_2O_5, the electrocatalytic performances were improved. This is presumably because, compared to bare V_2O_5, the AC-V_2O_5 composites have a higher density of the active sites and a lower electrical resistance, as discussed later. To clarify the above hypothesis, firstly, we calculated and compared the electrochemically active surface areas (ECSA) for both samples using the below equations [8, 9, 67, 68]:

$$J_{DL} = C_{DL} \times \frac{\nu}{A}, \quad (1)$$

$$\mathrm{ECSA} = \frac{C_{DL}}{C_e}, \quad (2)$$

where C_{DL}, C_e, A, J_{DL}, and ν are the non-Faradic capacitance, KOH electrolyte capacitance (0.04 mF/cm^2), electrode area, double-layer charging current, and scan rate, respectively. The ECSA values could be determined from the non-Faradic regions from 0 to 0.1 V in the CV curves of the V_2O_5 and AC-V_2O_5 catalysts (see also Figures S5(a) and S5(b)). Figures 5(c) and 5(d) display the linear relationship between J_{DL} and ν for V_2O_5 and AC-V_2O_5, respectively, which were extracted from the non-Faradic CV region at the potential of 0.05 V. From the slopes in Figures 5(c) and 5(d), the magnitudes of C_{DL} were determined to be 7.16 and 11.40 mF/cm^2 for V_2O_5 and AC-V_2O_5, respectively. According to the above equations, the obtained C_{DL} values correspond to ECSA of 179 and 285 cm^2 for V_2O_5 and AC-V_2O_5, respectively. This validates that the AC-V_2O_5 nanocomposites have a higher density of electrochemically active sites than that of the bare V_2O_5 nanorods.

Next, we assessed the electrocatalytic OER performances of V_2O_5 and AC-V_2O_5 by measuring their LSV characteristics. Figure 6(a) displays the i_R-corrected LSV characteristic curves of V_2O_5 and AC-V_2O_5 measured under 1 mV/s (see Figure S6(a) for the bare AC case). From the LSV data, the magnitudes of overpotential (η) were calculated to be 310, 280, and 230 mV (at 10 mA/cm^2) for V_2O_5,

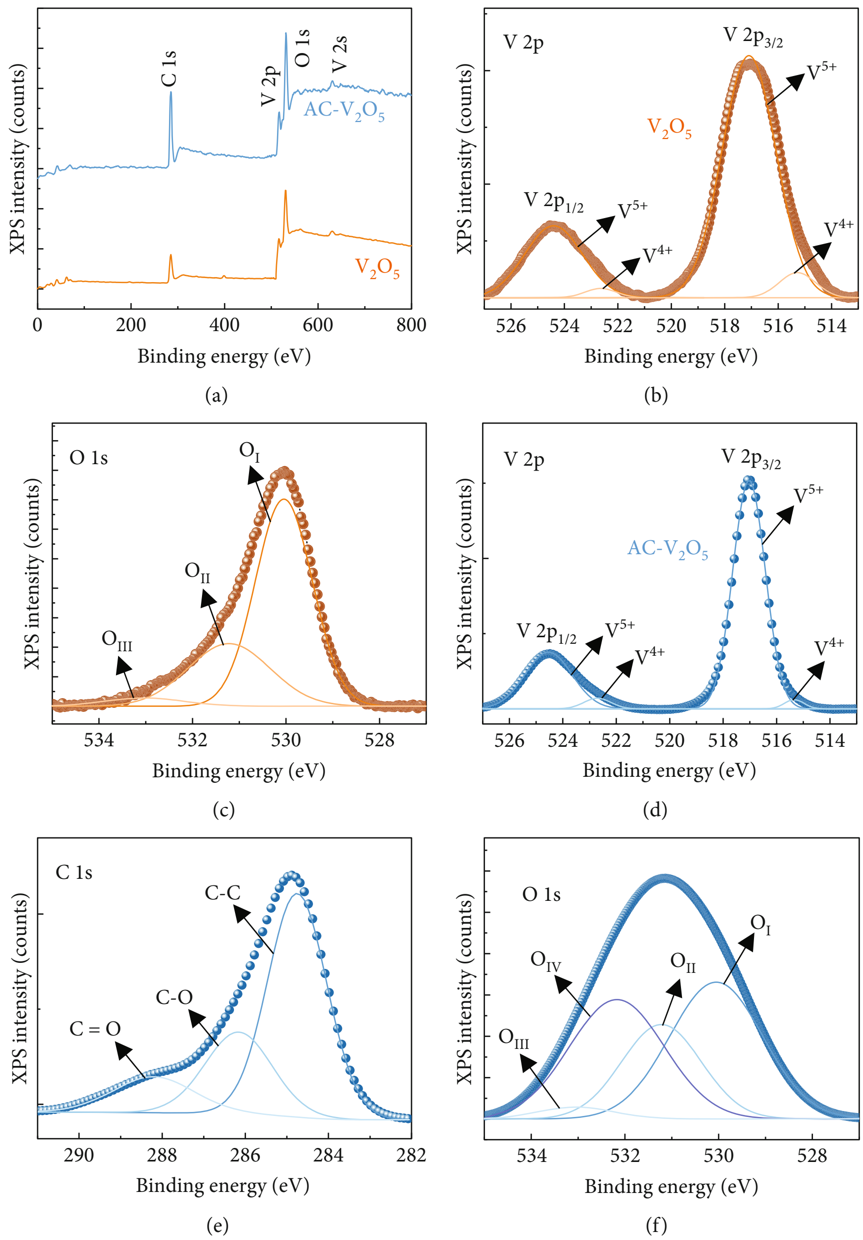

Figure 4: (a) Full survey XPS spectra of the V_2O_5 nanorods and the AC-V_2O_5 nanocomposites. (b) V 2p and (c) O 1s core-level spectra of the V_2O_5 nanorods. (d) V 2p, (e) C 1s, and (f) O 1s core-level spectra of the AC-V_2O_5 nanocomposites.

AC, and AC-V_2O_5, respectively, by using the following equations [5, 11]:

$$E_{\mathrm{RHE}} = E_{\mathrm{SCE}} + 0.059\mathrm{pH} + E^{0}{}_{\mathrm{SCE}}, \qquad (3)$$

$$\eta = E_{\mathrm{RHE}} - 1.23\ \mathrm{V}, \qquad (4)$$

where E_{RHE} and $E^{0}{}_{\mathrm{SCE}}$ are the standard potentials of the reversible hydrogen electrodes and the SCE at room temperature, respectively. Compared to bare V_2O_5, the AC-V_2O_5 nanocomposites exhibited a lower η value because of their increased electrocatalytically active sites (i.e., higher ECSA). Furthermore, the AC-V_2O_5 nanocomposites chronicled to possess the lowest η, compared to other metal oxide-based electrocatalysts (Table 1). The improved electrocatalytic OER kinetics could be further elucidated through calculating the magnitude of the Tafel slope (S_T) by using the following equation [9]:

$$\eta = S_{\mathrm{T}} \log (J) + a, \qquad (5)$$

where J and a are the applied current density and the fitting parameter, respectively. As can be seen from Figure 6(b), the Tafel slope was more gentle for AC-V_2O_5 than those for V_2O_5 and AC (see Figure S6(b)). Accordingly, a smaller S_{T} value was obtained from AC-V_2O_5 (i.e., 54 mV/dec), compared to V_2O_5 (i.e., 178 mV/dec) and AC (i.e., 68 mV/dec). Moreover, the S_{T} value of AC-V_2O_5 was smaller than

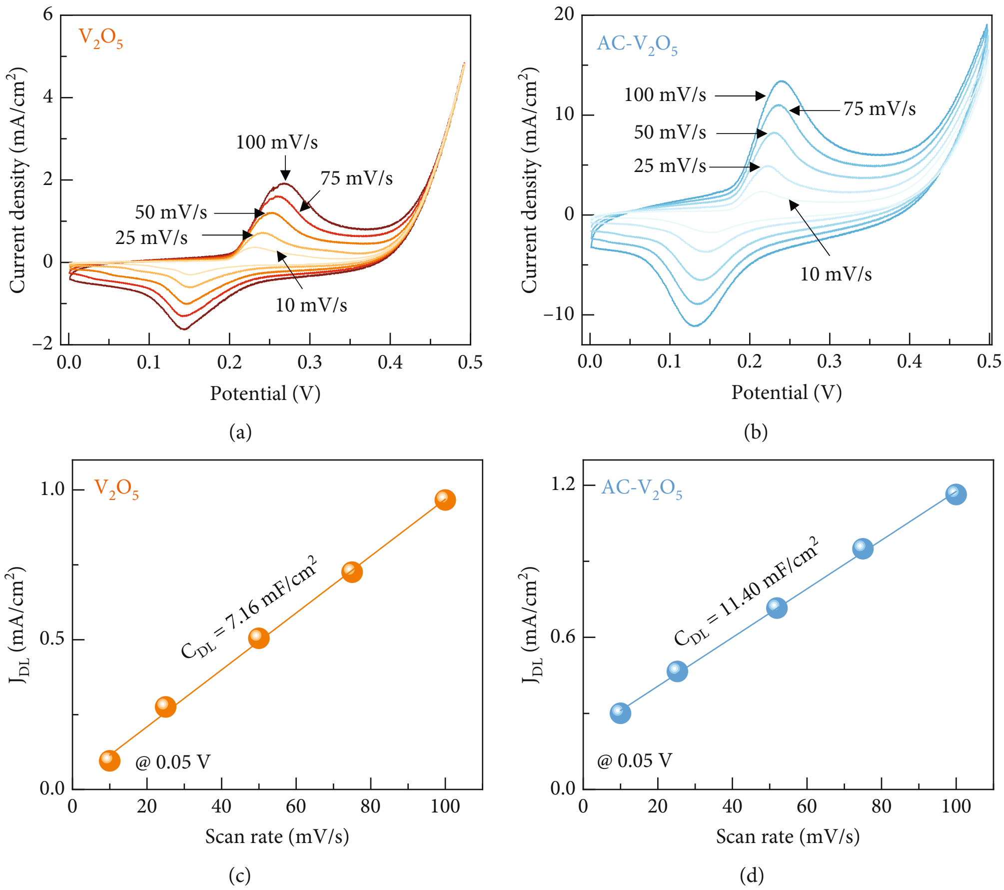

Figure 5: CV curves of the (a) V_2O_5 and the (b) AC-V_2O_5 catalysts performed by different scan rates of 10 to 100 mV/s. J_{DL} as a function of the scan rate at the potential of 0.05 V for the (c) V_2O_5 and the (d) AC-V_2O_5 catalysts.

that of other metal oxide-based electrocatalysts (Table 1). The obtained S_T value suggests that the AC-V_2O_5 catalyst follows the combined Volmer-Heyrovsky mechanism [32]. Compared to V_2O_5, AC-V_2O_5 exhibited the lower values of η and S_T because the AC-V_2O_5 hybridization in the composite system facilitates the enhanced catalytically active surface area and improves the material conductivity. Namely, the increased electrochemically active sites and the increased electrical conductivity eventually gave rise to the improved rate of the reaction kinetics. This hypothesis could also be corroborated by the ECSA-corrected LSV curve analysis (see Figure S7).

The improved electrocatalytic OER characteristics can also affect the CP performances. Figure 6(c) displays the CP profiles of the prepared catalysts. Compared to bare V_2O_5, the AC-V_2O_5 nanocomposites exhibited the smaller η values at every current density. This rarifies that the hybridization of AC with V_2O_5 could lead to improved catalytic activity because of the synergistic effects from both AC (i.e., high electrical conductivity) and V_2O_5 (i.e., high electrochemical activity). Additionally, AC-V_2O_5 showed better long-term stability than bare V_2O_5 (Figure 6(d)). Although both catalysts showed the stable potential profiles even after 20 h, AC-V_2O_5 revealed a smaller potential value, compared to bare V_2O_5. Furthermore, it was confirmed that the LSV curves were maintained to be nearly same before and after 20 h of the OER stability test (see Figure S8). Such a good long-term stability of AC-V_2O_5 could be attributed to the encapsulation of the V_2O_5 surface by AC. Namely, the chemically inert AC nanosheets that were physisorpted onto the V_2O_5 surface could improve the surface stability of V_2O_5 in the AC-V_2O_5 medium. This would eventually improve the long-term stability during the electrochemical reaction. All the above suggest that the AC-V_2O_5 composites hold superior electrocatalytic OER activity, compared to the bare V_2O_5 nanorods. After the OER stability test, we performed the Raman and FE-SEM measurements to observe the changes in both vibrational and microstructural characteristics of the catalysts. From FE-SEM measurements, the V_2O_5 catalyst showed the aggregated structure of the nanorods (see Figure S9(a)). However, the AC-V_2O_5 catalyst still maintained its original structure of the AC nanosheet-decorated V_2O_5 nanocomposites (see Figure S9(b)). From Raman measurements (see Figure S10), both V_2O_5 and AC-V_2O_5 showed the additional vibrational bands located at 294, 411, and 694 cm^{-1}, arising from the electrocatalytically active VOOH phase formed during the OER process [69].

Finally, we evaluated the resistive behaviors of the catalysts by means of the EIS measurements. Figures 7(a) and 7(b) show the Nyquist plots of the bare V_2O_5 nanorods and the AC-V_2O_5 composites, respectively. Both catalysts

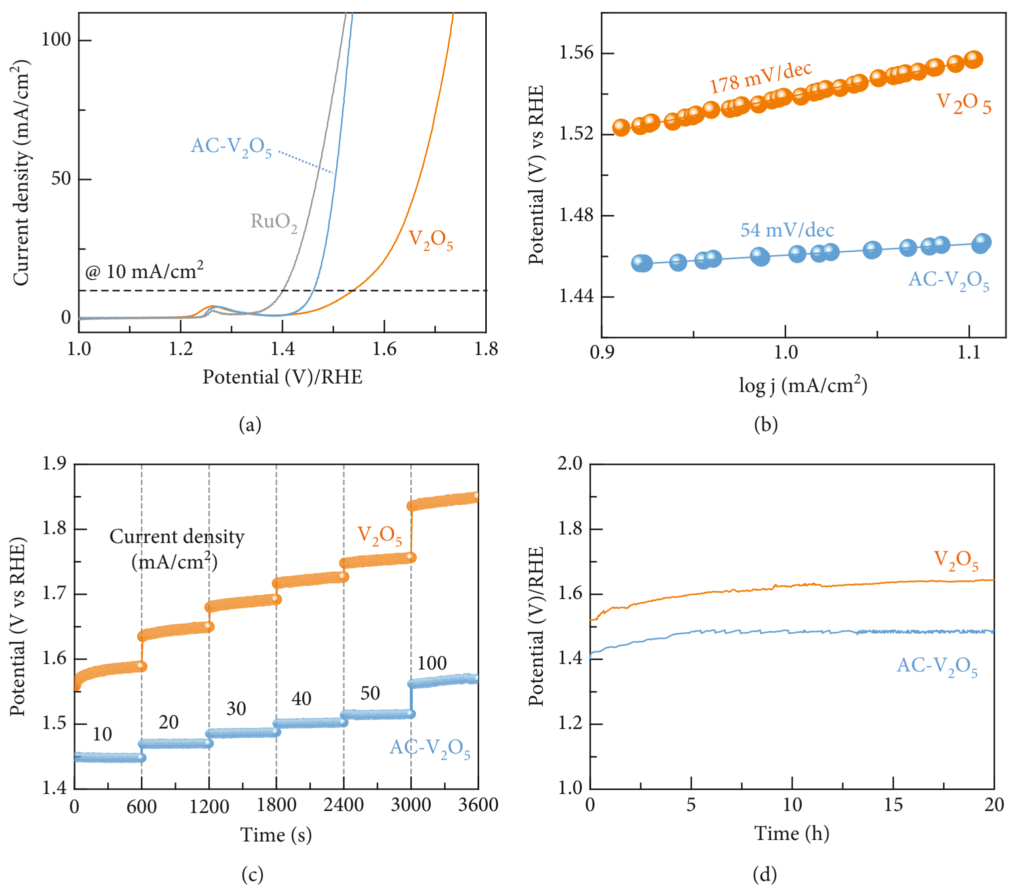

FIGURE 6: OER performances: (a) i_R-corrected LSV curves, (b) Tafel plots, (c) CP profiles at different current densities of 10 to 100 mA/cm^2 of the V_2O_5 and the AC-V_2O_5 catalysts, and (d) CP OER stability of the V_2O_5 and the AC-V_2O_5 catalysts measured up to 20 h at 10 mA/cm^2. The gray curve in (a) was measured from commercial RuO_2 to compare our results with the well-known standard catalyst.

TABLE 1: Comparison of the OER activities for the V_2O_5 and AC-V_2O_5 catalysts with previously reported metal oxide-based electrocatalysts.

Catalyst	Current density (mA/cm^2)	Overpotential η (mV)	Tafel slope (mV/dec)	Electrolyte	Reference
AC-V_2O_5	10	230	54	1 M KOH	This work
V_2O_5	10	310	178	1 M KOH	This work
V_2O_5/CFP	10	528	131	1 M KOH	[11]
Polycrystalline V_2O_5	10	310	88	1 M KOH	[17]
MOF-V_2O_5	50	430	50.3	1 M KOH	[71]
$Co_2V_2O_7$	10	340	62	1 M KOH	[72]
AC-NiO	10	320	49	1 M KOH	[41]
Co_3O_4/N-rmGO	10	310	67	1 M KOH	[73]
CNT-La$(OH)_3$	10	310	39	1 M KOH	[5]
Fe-doped $Co_3V_2O_8$	10	307	36	1 M KOH	[74]
WO_3/B-AC	10	320	48	1 M KOH	[9]
MoO_3/Ni-NiO	100	347	96	1 M KOH	[75]
NiCo LDH	10	367	40	1 M KOH	[76]
Fe_3O_4@Co_9S_8/rGO	10	320	54.5	1 M KOH	[77]
VO_x/Ni_3S_2	10	358	82	1 M KOH	[78]
d-Ti_3C_2/V_2O_5	10	240	52	1 M KOH	[10]
CoV_2O_6-V_2O_5/NRGO	10	239	49.7	1 M KOH	[35]

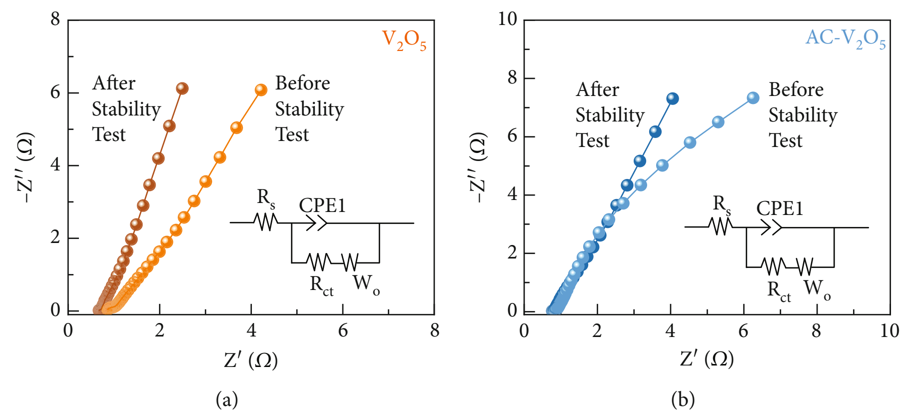

Figure 7: Nyquist plots of the (a) V_2O_5 and (b) AC-V_2O_5 catalysts before and after stability test. The inset in each figure represents the equivalent circuit of the working electrode.

clearly revealed the linear features at the low frequency region, attributing to the electrolyte diffusion within the catalyst medium [10, 15]. At the high frequency region, however, the samples exhibited no clear semicircles but revealed only small parabolic curvatures, which are associated with the charge transfer resistance (R_{ct}) [70]. By calculating the R_s and R_{ct} values using an equivalent circuit model (Figure 7, insets), it was found out that, compared to V_2O_5 (R_s: 0.86 Ω, R_{ct}: 83 mΩ), AC-V_2O_5 has smaller resistance values (R_s: 0.84 Ω, R_{ct}: 51 mΩ; see also Table S1). Consequently, it can be inferred that the outstanding OER performances of AC-V_2O_5 were attributed to both higher electrical conductivity (i.e., smaller R_s and R_{ct}) and higher ion storage capacity (i.e., greater ECSA), both of which give rise to the vigorous electrocatalytic OER actions inside the AC-V_2O_5-hybridized nanocomposite system.

4. Conclusions

The high-performance OER electrocatalyst of AC-V_2O_5 was fabricated by the facile hydrothermal reassembly process using the hydrothermally disassembled orthorhombic V_2O_5 nanorods and the rice husk-derived biomass AC nanosheets. The AC-V_2O_5 nanocomposites exhibited the outstanding OER performances in the 0.1 M KOH alkaline electrolyte. For example, a low η of 230 mV and a small S_T of 54 mV/dec were observed from the AC-V_2O_5 nanocomposites. These could be attributed to both higher ion storage capacity (ECSA: 285 cm^2) and high electrical conductivity (R_s: 0.84 Ω, R_{ct}: 51 mΩ), resulting from the synergistic hybridization of electrochemically active V_2O_5 and electrically conductive AC. Consequently, it can be concluded that the hydrothermally reassembled AC-V_2O_5 nanocomposites hold significant promise for future electrocatalytic water-splitting applications.

Data Availability

Data will be made available on request.

Conflicts of Interest

The authors declare that they have no known competing financial interests or personal relationships that could have appeared to influence the work reported in this paper.

Authors' Contributions

Sankar Sekar contributed to the investigation, formal analysis, methodology, and writing of the original draft. Pugazhendi Ilanchezhiyan assisted in the formal analysis and validation. Abu Talha Aqueel Ahmed carried out the investigation and formal analysis. Youngmin Lee made great contributions to the supervision, validation, and data curation. Sejoon Lee contributed to the conceptualization, supervision, and funding acquisition and wrote, reviewed, and edited the manuscript.

Acknowledgments

This research was supported by National Research Foundation (NRF) of Korea through the basic science research programs (2016R1A6A1A03012877 and 2023R1A2C1005421) funded by the Korean Government.

Supplementary Materials

Supplementary data includes the microstructural characteristics of the V_2O_5 bulk and AC nanosheets, the structural properties of the AC nanosheets, the electrocatalytic properties of V_2O_5 and AC-V_2O_5, the morphological properties of V_2O_5 and AC-V_2O_5 after the stability test, the structural properties of V_2O_5 and AC-V_2O_5 after the stability test, and the resistance parameters of V_2O_5 and AC-V_2O_5. Figure S1: FE-SEM image of the V_2O_5 bulk. Figure S2: FE-SEM image of the rice husk-derived biomass AC nanosheets. Figure S3: XRD pattern of the rice husk-derived biomass AC nanosheets. Figure S4: Raman spectra of the rice husk-derived biomass AC nanosheets. Figure S5: non-Faradic CV curves of the (a) V_2O_5 and the (b) AC-V_2O_5 catalysts. Figure S6: (a) LSV curve and (b) Tafel slope of the bare AC nanosheets. Figure S7: ECSA-normalized LSV curves of the (a) V_2O_5 and the (b) AC-V_2O_5 catalysts. Figure S8: LSV curves of the (a) V_2O_5 and the (b) AC-V_2O_5 before and after the OER stability test. Figure S9: FE-SEM images of the (a) V_2O_5 and the (b) AC-V_2O_5 catalysts after the stability test. Figure S10: Raman spectra of the (a) V_2O_5 and the (b) AC-V_2O_5 catalysts after the stability test. Table S1: fitted parameters from the Nyquist EIS curves of the V_2O_5 and AC-V_2O_5 catalysts. *(Supplementary Materials)*

References

[1] S. Chu and A. Majumdar, "Opportunities and challenges for a sustainable energy future," *Nature*, vol. 488, no. 7411, pp. 294–303, 2012.

[2] C. Jiang, J. Ma, G. Corre, S. L. Jain, and J. T. S. Irvine, "Challenges in developing direct carbon fuel cells," *Chemical Society Reviews*, vol. 46, no. 10, pp. 2889–2912, 2017.

[3] H. Singh, M. Marley-Hines, S. Chakravarty, and M. Nath, "Multi-walled carbon nanotube supported manganese selenide as a highly active bifunctional OER and ORR electrocatalyst," *Journal of Materials Chemistry A*, vol. 10, no. 12, pp. 6772–6784, 2022.

[4] Q. Hassan, A. Z. Sameen, H. M. Salman, M. Jaszczur, and A. K. Al-Jiboory, "Hydrogen energy future: advancements in storage technologies and implications for sustainability," *Journal of Energy Storage*, vol. 72, article 108404, 2023.

[5] S. Sekar, S. Park, J. Jung, and S. Lee, "Superb bifunctional water electrolysis activities of carbon nanotube-decorated lanthanum hydroxide nanocomposites," *International Journal of Energy Research*, vol. 2023, Article ID 6685726, 13 pages, 2023.

[6] M. Chatenet, B. G. Pollet, D. R. Dekel et al., "Water electrolysis: from textbook knowledge to the latest scientific strategies and industrial developments," *Chemical Society Reviews*, vol. 51, no. 11, pp. 4583–4762, 2022.

[7] S. Jiao, X. Fu, S. Wang, and Y. Zhao, "Perfecting electrocatalysts via imperfections: towards the large-scale deployment of water electrolysis technology," *Energy & Environmental Science*, vol. 14, no. 4, pp. 1722–1770, 2021.

[8] C. C. L. McCrory, S. Jung, J. C. Peters, and T. F. Jaramillo, "Benchmarking heterogeneous electrocatalysts for the oxygen evolution reaction," *Journal of the American Chemical Society*, vol. 135, no. 45, pp. 16977–16987, 2013.

[9] S. Sekar, A. T. Aqueel Ahmed, S. M. Pawar et al., "Enhanced water splitting performance of biomass activated carbon-anchored WO_3 nanoflakes," *Applied Surface Science*, vol. 508, article 145127, 2020.

[10] I. Ashraf, S. Ahmad, F. Nazir et al., "Hydrothermal synthesis and water splitting application of d-Ti_3C_2 MXene/V_2O_5 hybrid nanostructures as an efficient bifunctional catalyst," *International Journal of Hydrogen Energy*, vol. 47, no. 64, pp. 27383–27396, 2022.

[11] Y.-H. Choi, "VO_2 as a highly efficient electrocatalyst for the oxygen evolution reaction," *Nanomaterials*, vol. 12, no. 6, p. 939, 2022.

[12] F. Song, L. Bai, A. Moysiadou et al., "Transition metal oxides as electrocatalysts for the oxygen evolution reaction in alkaline solutions: an application-inspired renaissance," *Journal of the American Chemical Society*, vol. 140, no. 25, pp. 7748–7759, 2018.

[13] A. H. Al-Naggar, N. M. Shinde, J.-S. Kim, and R. S. Mane, "Water splitting performance of metal and non-metal-doped transition metal oxide electrocatalysts," *Coordination Chemistry Reviews*, vol. 474, article 214864, 2023.

[14] C. Youn, S. Shin, K. Shin et al., "Template-assisted synthesis of single-atom catalysts supported on highly crystalline vanadium pentoxide for stable oxygen evolution," *Chem Catalysis*, vol. 2, no. 5, pp. 1191–1210, 2022.

[15] F. Jafari and F. R. Rahsepar, "V_2O_5–Fe_3O_4/rGO ternary nanocomposite with dual applications as a dye degradation photocatalyst and OER electrocatalyst," *ACS Omega*, vol. 8, no. 38, pp. 35427–35439, 2023.

[16] J. Zhang, H. Zhang, M. Liu, Q. Xu, H. Jiang, and C. Li, "Cobalt-stabilized oxygen vacancy of V_2O_5 nanosheet arrays with delocalized valence electron for alkaline water splitting," *Chemical Engineering Science*, vol. 227, article 115915, 2020.

[17] V. Mounasamy, G. Srividhya, and N. Ponpandian, "Well-defined 2D transition vanadium pentoxide (V_2O_5) flat nanorods with large-scale synthesis feasibility as an electrocatalyst for the oxygen evolution reaction (OER)," *Energy Advances*, vol. 2, no. 6, pp. 784–788, 2023.

[18] S. Sekar, I. Rabani, C. Bathula et al., "Graphitic carbon-encapsulated V_2O_5 nanocomposites as a superb photocatalyst for crystal violet degradation," *Environmental Research*, vol. 205, article 112201, 2022.

[19] C.-J. Mao, H. C. Pan, X. C. Wu, J. J. Zhu, and H. Y. Chen, "Sonochemical route for self-assembled V_2O_5 bundles with spindle-like morphology and their novel application in serum albumin sensing," *The Journal of Physical Chemistry B*, vol. 110, no. 30, pp. 14709–14713, 2006.

[20] S. Tabatabai Yazdi, M. Mousavi, and G. H. Khorrami, "Effect of Co-doping in V_2O_5 nanoparticles synthesized via a gelatin-based sol-gel method," *Materials Today Communications*, vol. 26, article 101955, 2021.

[21] D. Huang, J. Huang, Y. Zhang, Y. Fan, and P. Hu, "Short-process preparation of high-purity V_2O_5 from shale acid leaching solution via chlorination," *Processes*, vol. 11, no. 4, p. 1270, 2023.

[22] R. Berenguer, M. O. Guerrero-Pérez, I. Guzmán, J. Rodríguez-Mirasol, and T. Cordero, "Synthesis of vanadium oxide nanofibers with variable crystallinity and V^{5+}/V^{4+} ratios," *ACS Omega*, vol. 2, no. 11, pp. 7739–7745, 2017.

[23] X. Liu, J. Zeng, H. Yang, K. Zhou, and D. Pan, "V_2O_5-based nanomaterials: synthesis and their applications," *RSC Advances*, vol. 8, no. 8, pp. 4014–4031, 2018.

[24] P. Taylor, M. Kusper, T. Hesabizadeh et al., "Synthesis of naked vanadium pentoxide nanoparticles," *Nanoscale Advances*, vol. 3, no. 7, pp. 1954–1961, 2021.

[25] Z. Yin, J. Xu, Y. Ge et al., "Synthesis of V_2O_5 microspheres by spray pyrolysis as cathode material for supercapacitors," *Materials Research Express*, vol. 5, no. 3, article 036306, 2018.

[26] S. K. Jayaraj, V. Sadishkumar, T. Arun, and P. Thangadurai, "Enhanced photocatalytic activity of V_2O_5 nanorods for the photodegradation of organic dyes: a detailed understanding of the mechanism and their antibacterial activity," *Materials Science in Semiconductor Processing*, vol. 85, pp. 122–133, 2018.

[27] J. Mu, J. Wang, J. Hao et al., "Hydrothermal synthesis and electrochemical properties of V_2O_5 nanomaterials with different dimensions," *Ceramics International*, vol. 41, no. 10, Part A, pp. 12626–12632, 2015.

[28] M. Lee, S. K. Balasingam, H. Y. Jeong et al., "One-step hydrothermal synthesis of graphene decorated V_2O_5 nanobelts for

enhanced electrochemical energy storage," *Surfaces and Interfaces*, vol. 5, no. 1, p. 8151, 2015.

[29] S. Lee, J. Kim, J. H. Jeon et al., "Chemical vapor-deposited vanadium pentoxide nanosheets with highly stable and low switching voltages for effective selector devices," *ACS Applied Materials & Interfaces*, vol. 10, no. 49, pp. 42875–42881, 2018.

[30] P. Hu, P. Hu, T. D. Vu et al., "Vanadium oxide: phase diagrams, structures, synthesis, and applications," *Chemical Reviews*, vol. 123, no. 8, pp. 4353–4415, 2023.

[31] A. Varghese, K. R. Sunaja Devi, D. Pinheiro, and M. K. Mohan, "Molecular architecture of PANI/V_2O_5/MnO_2 composite designed for hydrogen evolution reaction," *Surfaces and Interfaces*, vol. 41, article 103221, 2023.

[32] A. Meena, M. Ha, S. S. Chandrasekaran et al., "Pt-like hydrogen evolution on a V_2O_5/Ni$(OH)_2$ electrocatalyst," *Journal of Materials Chemistry A*, vol. 7, no. 26, pp. 15794–15800, 2019.

[33] Z. Yang, X. Xie, Z. Zhang et al., "NiS_2@V_2O_5/VS_2 ternary heterojunction for a high-performance electrocatalyst in overall water splitting," *International Journal of Hydrogen Energy*, vol. 47, no. 64, pp. 27338–27346, 2022.

[34] Y. Wu, G. Gao, and G. Wu, "Self-assembled three-dimensional hierarchical porous V_2O_5/graphene hybrid aerogels for supercapacitors with high energy density and long cycle life," *Journal of Materials Chemistry A*, vol. 3, no. 5, pp. 1828–1832, 2015.

[35] F.-C. Shen, Y. Wang, Y.-J. Tang et al., "CoV_2O_6–V_2O_5 coupled with porous N-doped reduced graphene oxide composite as a highly efficient electrocatalyst for oxygen evolution," *ACS Energy Letters*, vol. 2, no. 6, pp. 1327–1333, 2017.

[36] G. Sun, H. Ren, Z. Shi et al., "V_2O_5/vertically-aligned carbon nanotubes as negative electrode for asymmetric supercapacitor in neutral aqueous electrolyte," *Journal of Colloid and Interface Science*, vol. 588, pp. 847–856, 2021.

[37] T. Munawar, A. Bashir, M. S. Nadeem et al., "Scalable synthesis of MOF-derived Nd_2O_3@C and V_2O_5@C nanohybrid: efficient electrocatalyst for OER in alkaline medium," *Fuel*, vol. 355, article 129485, 2024.

[38] R. Manikandan, S. Sadhasivam, S. Lee et al., "Deep eutectic solvents assisted synthesis of AC-decorated NiO nanocomposites for hydrogen evolution reaction," *Journal of Molecular Liquids*, vol. 375, article 121338, 2023.

[39] P. Feng, J. Li, H. Wang, and Z. Xu, "Biomass-based activated carbon and activators: preparation of activated carbon from corncob by chemical activation with biomass pyrolysis liquids," *ACS Omega*, vol. 5, no. 37, pp. 24064–24072, 2020.

[40] S. Sekar, A. T. Aqueel Ahmed, D. H. Sim, and S. Lee, "Extraordinarily high hydrogen-evolution-reaction activity of corrugated graphene nanosheets derived from biomass rice husks," *International Journal of Hydrogen Energy*, vol. 47, no. 95, pp. 40317–40326, 2022.

[41] S. Sekar, D. Kim, and S. Lee, "Excellent oxygen evolution reaction of activated carbon-anchored NiO nanotablets prepared by green routes," *Nanomaterials*, vol. 10, no. 7, p. 1382, 2020.

[42] S. Sekar, V. Preethi, S. Saravanan, D. Y. Kim, and S. Lee, "Excellent photocatalytic performances of Co_3O_4–AC nanocomposites for H_2 production via wastewater splitting," *Chemosphere*, vol. 286, article 131823, Part 2, 2022.

[43] J. Serafin, B. Dziejarski, O. F. Cruz Junior, and J. Sreńscek-Nazzal, "Design of highly microporous activated carbons based on walnut shell biomass for H_2 and CO_2 storage," *Carbon*, vol. 201, pp. 633–647, 2023.

[44] S. Sankar, H. Lee, H. Jung et al., "Ultrathin graphene nanosheets derived from rice husks for sustainable supercapacitor electrodes," *New Journal of Chemistry*, vol. 41, no. 22, pp. 13792–13797, 2017.

[45] L. Luo, Y. Lan, Q. Zhang et al., "A review on biomass-derived activated carbon as electrode materials for energy storage supercapacitors," *Journal of Energy Storage*, vol. 55, article 105839, 2022.

[46] J. Livage, "Hydrothermal synthesis of nanostructured vanadium oxides," *Materials*, vol. 3, no. 8, pp. 4175–4195, 2010.

[47] N. Sahraeian, F. Esmaeilzadeh, and D. Mowla, "Hydrothermal synthesis of V_2O_5 nanospheres as catalyst for hydrogen sulfide removal from sour water," *Ceramics International*, vol. 47, no. 1, pp. 923–934, 2021.

[48] W. Yu, J. Wang, Z. Gou, W. Zeng, W. Guo, and L. Lin, "Hydrothermal synthesis of vanadium pentoxide nanostructures and their morphology control," *Ceramics International*, vol. 39, no. 3, pp. 2639–2643, 2013.

[49] Q. An, Q. Wei, L. Mai et al., "Supercritically exfoliated ultrathin vanadium pentoxide nanosheets with high rate capability for lithium batteries," *Physical Chemistry Chemical Physics*, vol. 15, no. 39, pp. 16828–16833, 2013.

[50] A. S. Etman, A. J. Pell, P. Svedlindh et al., "Insights into the exfoliation process of $V_2O_5 \cdot nH_2O$ nanosheet formation using real-time ^{51}V NMR," *ACS Omega*, vol. 4, no. 6, pp. 10899–10905, 2019.

[51] S. Wang, T. Yu, Y. Li, H. Fu, and C. Sun, "General methods for large-scale production of nanostructured V_2O_5 with controlled morphologies," *Materials Research Bulletin*, vol. 111, pp. 284–288, 2019.

[52] S. K. Jayaraj and P. Thangadurai, "Surface decorated V_2O_5 nanorods with Pt nanoparticles for enriched visible light photocatalytic performance for the photodegradation of Rh-6G," *Journal of Molecular Liquids*, vol. 319, article 114368, 2020.

[53] M. Beaula Ruby Kamalam, S. S. R. Inbanathan, K. Sethuraman et al., "Direct sunlight-driven enhanced photocatalytic performance of V_2O_5 nanorods/graphene oxide nanocomposites for the degradation of Victoria blue dye," *Environmental Research*, vol. 199, article 111369, 2021.

[54] S. Kundu, B. Satpati, T. Kar, and S. K. Pradhan, "Microstructure characterization of hydrothermally synthesized PANI/$V_2O_5 \cdot nH_2O$ heterojunction photocatalyst for visible light induced photodegradation of organic pollutants and non-absorbing colorless molecules," *Journal of Hazardous Materials*, vol. 339, pp. 161–173, 2017.

[55] S. A. Alsherari, F. Janene, A. Moulahi, H. Shili, I. Alnhas, and I. Mjejri, "Vanadium oxide nanocomposite as electrode materials for lithium-ion batteries with high specific discharge capacity and long cycling life," *Ionics*, vol. 29, no. 1, pp. 61–70, 2023.

[56] D. Sharma, M. Faraz, D. Kumar, D. Takhar, B. Birajdar, and N. Khare, "Visible light activated V_2O_5/rGO nanocomposite for enhanced photodegradation of methylene blue dye and photoelectrochemical water splitting," *Inorganic Chemistry Communications*, vol. 142, article 109657, 2022.

[57] A. A. Yadav, Y. M. Hunge, S. W. Kang, A. Fujishima, and C. Terashima, "Enhanced photocatalytic degradation activity using the V_2O_5/RGO composite," *Nanomaterials*, vol. 13, no. 2, p. 338, 2023.

[58] T. Zhai, H. Liu, H. Li et al., "Centimeter-long V_2O_5 nanowires: from synthesis to field-emission, electrochemical, electrical

transport, and photoconductive properties," *Advanced Materials*, vol. 22, no. 23, pp. 2547–2552, 2010.

[59] V. Naydenov, L. Tosheva, and J. Sterte, "Spherical silica macrostructures containing vanadium and tungsten oxides assembled by the resin templating method," *Microporous and Mesoporous Materials*, vol. 55, no. 3, pp. 253–263, 2002.

[60] R. Baddour-Hadjean, V. Golabkan, J. P. Pereira-Ramos, A. Mantoux, and D. Lincot, "A Raman study of the lithium insertion process in vanadium pentoxide thin films deposited by atomic layer deposition," *Journal of Raman Specroscopy*, vol. 33, no. 8, pp. 631–638, 2002.

[61] A. Mishra, A. Panigrahi, P. Mal et al., "Rapid photodegradation of methylene blue dye by rGO-V_2O_5 nano composite," *Journal of Alloys and Compounds*, vol. 842, p. 155746, 2020.

[62] M. Shanmugam, A. Alsalme, A. Alghamdi, and R. Jayavel, "Enhanced photocatalytic performance of the graphene-V_2O_5 nanocomposite in the degradation of methylene blue dye under direct sunlight," *ACS Applied Materials & Interfaces*, vol. 7, no. 27, pp. 14905–14911, 2015.

[63] M. Sathiya, A. S. Prakash, K. Ramesha, J.-M. Tarascon, and A. K. Shukla, "V_2O_5-anchored carbon nanotubes for enhanced electrochemical energy storage," *Journal of the American Chemical Society*, vol. 133, no. 40, pp. 16291–16299, 2011.

[64] A.-Y. Wang, M. Chaudhary, and T.-W. Lin, "Enhancing the stability and capacitance of vanadium oxide nanoribbons/3D-graphene binder-free electrode by using $VOSO_4$ as redox-active electrolyte," *Chemical Engineering Journal*, vol. 355, pp. 830–839, 2019.

[65] H. Mustafa, Y. Yu, A. Zafar et al., "MWCNT synergy for boosting the electrochemical kinetics of V_2O_5 cathode for lithium-ion batteries," *New Journal of Chemistry*, vol. 46, no. 7, pp. 3417–3425, 2022.

[66] H. Guedidi, L. Reinert, Y. Soneda, N. Bellakhal, and L. Duclaux, "Adsorption of ibuprofen from aqueous solution on chemically surface-modified activated carbon cloths," *Arabian Journal of Chemistry*, vol. 10, pp. S3584–S3594, 2017.

[67] S. Sekar, S. Sadhasivam, E. K. Nangai, S. Saravanan, D. Y. Kim, and S. Lee, "Enhanced hydrogen evolution reaction performances of ultrathin $CuBi_2O_4$ nanoflakes," *International Journal of Energy Research*, vol. 2023, Article ID 5038466, 10 pages, 2023.

[68] M. Guo, S. Song, S. Zhang et al., "Fe-doped Ni–Co phosphide nanoplates with planar defects as an efficient bifunctional electrocatalyst for overall water splitting," *ACS Sustainable Chemistry & Engineering*, vol. 8, no. 19, pp. 7436–7444, 2020.

[69] H. Shi, H. Liang, F. Ming, and Z. Wang, "Efficient overall water-splitting electrocatalysis using lepidocrocite VOOH hollow nanospheres," *Angewandte Chemie, International Edition*, vol. 56, no. 2, pp. 573–577, 2017.

[70] J. Tang, Q. Ruan, H. Yu, and C. Huang, "Activating $Co(OH)_2$ Active sites by coupled with V_2O_5 to boost highly efficient oxygen evolution reaction," *Advanced Sustainable Systems*, vol. 7, no. 5, article 2200473, 2023.

[71] S.-M. Ji, A. Muthurasu, K. Chhetri, and H. Yong Kim, "Metal-organic framework assisted vanadium oxide nanorods as efficient electrode materials for water oxidation," *Journal of Colloid and Interface Science*, vol. 618, pp. 475–482, 2022.

[72] X. Peng, L. Wang, L. Hu et al., "In situ segregation of cobalt nanoparticles on VN nanosheets via nitriding of $Co_2V_2O_7$ nanosheets as efficient oxygen evolution reaction electrocatalysts," *Nano Energy*, vol. 34, pp. 1–7, 2017.

[73] Y. Liang, Y. Li, H. Wang et al., "Co_3O_4 nanocrystals on graphene as a synergistic catalyst for oxygen reduction reaction," *Nature Materials*, vol. 10, no. 10, pp. 780–786, 2011.

[74] T. Gao, Z. Jin, M. Liao, J. Xiao, H. Yuan, and D. Xiao, "A trimetallic V–Co–Fe oxide nanoparticle as an efficient and stable electrocatalyst for oxygen evolution reaction," *Journal of Materials Chemistry A*, vol. 3, no. 34, pp. 17763–17770, 2015.

[75] X. Li, Y. Wang, J. Wang et al., "Sequential electrodeposition of bifunctional catalytically active structures in MoO_3/Ni–NiO composite electrocatalysts for selective hydrogen and oxygen evolution," *Advanced Materials*, vol. 32, no. 39, article 2003414, 2020.

[76] H. Liang, F. Meng, M. Cabán-Acevedo et al., "Hydrothermal continuous flow synthesis and exfoliation of NiCo layered double hydroxide nanosheets for enhanced oxygen evolution catalysis," *Nano Letters*, vol. 15, no. 2, pp. 1421–1427, 2015.

[77] J. Yang, G. Zhu, Y. Liu et al., "Fe_3O_4-decorated Co_9S_8 Nanoparticles in situ grown on reduced graphene oxide: a new and efficient electrocatalyst for oxygen evolution reaction," *Advanced Functional Materials*, vol. 26, no. 26, pp. 4712–4721, 2016.

[78] Y. Niu, W. Li, X. Wu et al., "Amorphous nickel sulfide nanosheets with embedded vanadium oxide nanocrystals on nickel foam for efficient electrochemical water oxidation," *Journal of Materials Chemistry A*, vol. 7, no. 17, pp. 10534–10542, 2019.